PLOS ONE

RESEARCH ARTICLE

Brain functional BOLD perturbation modelling for forward fMRI and inverse mapping

Zikuan Chen[1]*, Jennifer Robinson[2,3], Vince Calhoun[1,4]

1 The Mind Research Network and LBERI, Albuquerque, New Mexico, United States of America, **2** Department of Psychology, Auburn University, Auburn, Alabama, United States of America, **3** Auburn University MRI Research Center, Auburn University, Auburn, Alabama, United States of America, **4** University of New Mexico, Depart Electrical Computer Engineering, Albuquerque, New Mexico, United States of America

* zchen@mrn.org

Citation: Chen Z, Robinson J, Calhoun V (2018) Brain functional BOLD perturbation modelling for forward fMRI and inverse mapping. PLoS ONE 13 (1): e0191266. https://doi.org/10.1371/journal.pone.0191266

Editor: Wang Zhan, University of Maryland at College Park, UNITED STATES

Received: May 21, 2017

Accepted: January 2, 2018

Published: January 19, 2018

Data Availability Statement: All relevant data are within the paper and its Supporting Information files.

Funding: The authors would like to acknowledge the funding support of NIHP20GM103472.

Competing interests: The authors have declared that no competing interests exist.

Abbreviations: BOLD, blood oxygenation level dependence; CIMRI, computed inverse magnetic resonance imaging; EPI, echo-planar imaging; *fmap*, functional map; fMRI, functional magnetic

Abstract

Purpose

To computationally separate dynamic brain functional BOLD responses from static background in a brain functional activity for forward fMRI signal analysis and inverse mapping.

Methods

A brain functional activity is represented in terms of magnetic source by a perturbation model: $\chi = \chi_0 + \delta\chi$, with $\delta\chi$ for BOLD magnetic perturbations and χ_0 for background. A brain fMRI experiment produces a timeseries of complex-valued images (T2* images), whereby we extract the BOLD phase signals (denoted by δP) by a complex division. By solving an inverse problem, we reconstruct the BOLD $\delta\chi$ dataset from the δP dataset, and the brain χ distribution from a (unwrapped) T2* phase image. Given a 4D dataset of task BOLD fMRI, we implement brain functional mapping by temporal correlation analysis.

Results

Through a high-field (7T) and high-resolution (0.5mm in plane) task fMRI experiment, we demonstrated in detail the BOLD perturbation model for fMRI phase signal separation ($P + \delta P$) and reconstructing intrinsic brain magnetic source (χ and $\delta\chi$). We also provided to a low-field (3T) and low-resolution (2mm) task fMRI experiment in support of single-subject fMRI study. Our experiments show that the $\delta\chi$-depicted functional map reveals bidirectional BOLD χ perturbations during the task performance.

Conclusions

The BOLD perturbation model allows us to separate fMRI phase signal (by complex division) and to perform inverse mapping for pure BOLD $\delta\chi$ reconstruction for intrinsic functional χ mapping. The full brain χ reconstruction (from unwrapped fMRI phase) provides a new brain tissue image that allows to scrutinize the brain tissue idiosyncrasy for the pure BOLD $\delta\chi$ response through an automatic function/structure co-localization.

resonance imaging; GRE, gradient-recalled echo; MRI, magnetic resonance imaging; QSM, quantitative susceptibility mapping; *tcorr*, temporal correlation.

Introduction

The blood oxygenation level-dependent (BOLD) signal [1–4] has been widely leveraged for neuroimaging studies using functional magnetic resonance imaging (fMRI). Through the use of a gradient-recalled echo (GRE) echo planar imaging (EPI) sequence and quadrature detection, the data acquisition of BOLD fMRI produces a timeseries of T2*-dephasing images, which are complex-valued in nature. Conventionally, we depict the brain functional map from the 4D T2* magnitude dataset, while discarding the 4D T2* phase dataset. However, the T2* phase conveys information concerning brain magnetic state that is different from the T2* magnitude [5,6]. Especially, the inverse mapping for brain magnetic source reconstruction can only be achieved via T2* phase rather than T2* magnitude [7–10]. The inverse mapping for BOLD fMRI seeks the dynamic BOLD magnetic source from the timeseries of T2* phase images [8].

A complex T2* image is formed by an intravoxel spin dephasing mechanism [6,8]. The image contrast is attributed to the origin of brain tissue heterogeneity in terms of inhomogeneous magnetic susceptibility property distribution that causes an inhomogeneous fieldmap via a tissue magnetization process in a main field B_0. For BOLD fMRI studies focusing on the brain, we are concerned with the original magnetism expression (in terms of intrinsic tissue magnetic property, prior to magnetization and other MRI transformations) of BOLD information conveyed in the T2* magnitude and phase datasets. A T2* image contains morphologic distortions and is nonlinearly related to the magnetic source [5,7,8]. Consequently, the timeseries of T2* magnitude or phase images have a complicated relationship to the original BOLD responses. These relationships have been numerically simulated [5,11–15]. Even so, the BOLD fMRI model remains incomplete, in particular in the magnetic expression of a neurovascular-coupled physiologically driven BOLD signal. By decomposing a brain magnetic state into a static background and a dynamic perturbation, we may look into the insights of BOLD fMRI for the static brain parenchymal and dynamic functional contributions and their inverse mappings separately.

Our recent research [8,16–19] has demonstrated that the T2* phase data can be used to reconstruct the original brain magnetic susceptibility source (denoted by χ). We propose using a BOLD perturbation model to describe the brain χ source in a decomposition of static brain parenchyma (denoted by χ_0) and dynamic BOLD perturbation (denoted by $\delta\chi$). With dynamic/static source separation, the dataflow during T2* imaging in an accompaniment of BOLD field perturbation and BOLD phase perturbation models can be shown. Our ultimate goal is to reconstruct the BOLD $\delta\chi$ dataset from the T2* phase dataset by solving an inverse imaging problem [20], achieving χ-depicted intrinsic brain functional mapping.

The fMRI signals are noisy and small (accounting for less than a 5% change in energy consumption [21,22]) such that a brain functional activity is indiscernible in a snapshot of brain imaging. For a task-evoked BOLD fMRI experiment, a designed task paradigm that consists of a repetition of stimuli is always used to deal with the BOLD signal weakness. While multi-subject population statistics are widely accepted for group-level BOLD fMRI studies, a research trend of using individual fMRI study has recently emerged under the claim that "data from a single subject are actually meaningful and reliable" [23,24]. Accordingly, we applied our BOLD perturbation model to two single-subject task fMRI experimental data analyses (one 7T high-resolution dataset and another 3T low-resolution one). Without group averaging, the single-subject experimental data analysis allows us 1) to examine the brain BOLD perturbation model in technical detail; 2) to observe the single subject's function idiosyncrasy; and 3) to co-localize a brain function map with its brain tissue structure (background) *per se*.

Theory, model and methods

The overview of BOLD fMRI and its inverse for brain functional χ mapping is shown in Fig 1, which consists of a cascade of three stages: (a) BOLD fMRI for data acquisition (T2* phase imaging); (b) Inverse mappings for δχ and χ source reconstructions; and (c) brain function/structure depictions in reconstructed δχ and χ source dataspaces.

The magnetic source of BOLD fMRI is a dynamic spatiotemporal distribution of brain tissue magnetic susceptibility (primarily the change in cerebral vascular blood magnetism), denoted by $\chi(\mathbf{r},t)$. Under MRI scanning (in a static field B_0) through the use of a GRE EPI sequence (with an echo time T_E), the BOLD fMRI data acquisition produces a timeseries of complex-valued T2* images, denoted by $C[\mathbf{r},t]$. With an additive BOLD perturbation model for the magnetic source $\chi(\mathbf{r},t)$, denoted by $\chi(\mathbf{r},t) = \chi_0(\mathbf{r}) + \delta\chi(\mathbf{r},t)$, we may extract the BOLD contribution in the T2* signal (in terms of phase changes $\delta P[\mathbf{r},t]$, see below) and retrospectively reconstruct the BOLD magnetic source (in terms of $\delta\chi[\mathbf{r},t]$) by performing inverse mapping. The ultimate goal is to depict brain functions in the reconstructed BOLD magnetic source dataspace ($\delta\chi[\mathbf{r},t]$). It is noted in Fig 1 that the BOLD fMRI data acquisition introduces the MRI parameters (such as B_0 and T_E) that are thereafter removed by inverse fMRI, and that the BOLD perturbation modeling enables both $\delta\chi[\mathbf{r},t]$ and $\chi[\mathbf{r},t]$ reconstructions. More details about this technique are addressed in the followings.

BOLD perturbation modeling for fMRI data acquisition

Let $\chi_0(\mathbf{r})$ denote a static brain tissue magnetic state, $\delta\chi(\mathbf{r},t)$, which is a dynamic brain BOLD activity in an expression of cerebral blood magnetism. We assume an additive perturbation model to describe the spatiotemporal evolution of brain χ states by

$$\begin{aligned} &\chi(\mathbf{r},t) = \chi_0(\mathbf{r}) + \delta\chi(\mathbf{r},t) \quad (\chi \text{ perturbation}) \\ &\text{with } |\delta\chi| << |\chi_0| \end{aligned} \tag{1}$$

The BOLD χ perturbation model in Eq (1) greatly simplifies the complicated neurovascular process associated with a brain biophysiological activity and is very useful for numerical BOLD fMRI simulations [5,7,14,15]. Herewith, we make use of the BOLD χ perturbation model presented in Eq (1) to trace the data flow of BOLD δχ source during BOLD fMRI data acquisition.

Placed in a main field B_0, the brain tissue is subject to a magnetization (magnetic polarization) process that manifests as a spatial orientation alignment of the magnetic dipole moments along B_0 (parallel for paramagnetic magnetization and antiparallel for diamagnetic magnetization). Since brain tissue is a nonmagnetic material (strictly, a weak magnetic material, with $|\chi| \sim 1\times10^{-6}$ in dimensionless unit in SI metric), the tissue magnetization can be linearly approximated [25] by

$$\begin{aligned} &\mu_0\mathbf{M}(\mathbf{r}) = \chi(\mathbf{r})\mathbf{B}_0 \text{ (linear magnetization)} \\ &\text{with } \mathbf{M}(\mathbf{r}) \equiv \frac{\sum_{\mathbf{r}\prime\in d^3\mathbf{r}} \mathbf{m}(\mathbf{r}\prime)}{|d^3\mathbf{r}|} \end{aligned} \tag{2}$$

where $\mathbf{m}(\mathbf{r})$ denotes a microscopic magnetic dipole moment, $\mathbf{M}(\mathbf{r})$ a macroscopic magnetization vector per macroscopic volume, $|d^3\mathbf{r}|$ a volume element, and $\mu_0 = 4\pi\times10^{-7}$ N/A^2, a magnetic constant (vaccum permeability). Under linear magnetization approximations, the

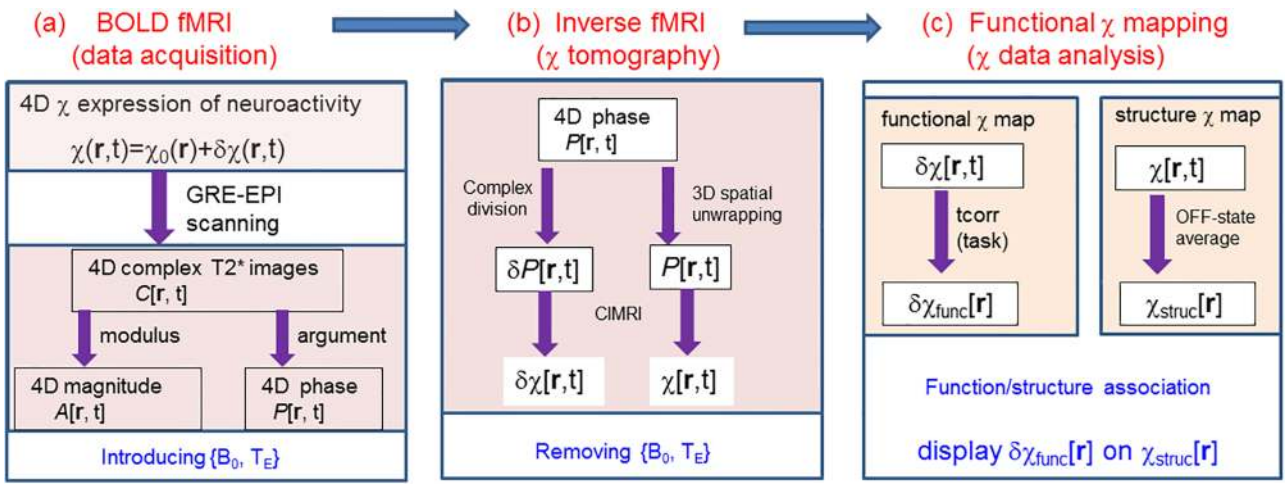

Fig 1. Overview diagram of BOLD perturbation model for brain imaging and functional mapping.

https://doi.org/10.1371/journal.pone.0191266.g001

χ-induced fieldmap is given by

$$\begin{aligned} b(\mathbf{r},t) &= B_0\chi(\mathbf{r},t) * h_{dipole}(\mathbf{r}) \qquad \text{(linear magnetization approx)} \\ \text{with } h_{\text{dipole}}(\mathbf{r}) &= \frac{1}{4\pi}\frac{3z^2-\mathbf{r}^2}{|\mathbf{r}|^5} \qquad \text{(dipole kernel)} \end{aligned} \tag{3}$$

where h_{diople} denotes the magnetic field distribution of a point magnetic dipole and $*$ denotes a 3D spatial convolution. Strictly viewed, $b(\mathbf{r},t)$ only represents the z-component of the 3D vector field (related to the 3D magnetization vector $\mathbf{M}$) at a time point t. Since the spatial convolution is a linear spatial transformation, the fieldmap resulting from $\chi(\mathbf{r},t)$ is given by

$$\begin{aligned} b(\mathbf{r},t) &= b_0(\mathbf{r}) + \delta b(\mathbf{r},t) \qquad \text{(fieldmap perturbation)} \\ \text{with } b_0(\mathbf{r}) &= B_0\chi_0(\mathbf{r}) * h_{dipole}(\mathbf{r}) \qquad \text{(static background)} \\ \delta b(\mathbf{r},t) &= B_0\delta\chi(\mathbf{r},t) * h_{dipole}(\mathbf{r}) \qquad \text{(BOLD portion)} \end{aligned} \tag{4}$$

That is, the intracranial fieldmap $b(\mathbf{r},t)$ consists of two parts: the static field background $b_0(\mathbf{r})$ and the dynamic BOLD field perturbation $\delta b(\mathbf{r},t)$. It is mentioned that $b(\mathbf{r},t)$ is linearly related to $\chi(\mathbf{r},t)$, so is $\delta b(\mathbf{r},t)$ to $\delta\chi(\mathbf{r},t)$ due to the additive decomposition.

The T2*MRI detection on a snapshot of the fieldmap $b(\mathbf{r},t)$ produces a complex-valued image (called a complex T2* image) by an intravoxel dephasing formula [5,15,26], as given by

$$\begin{aligned} C[\mathbf{r},t] &= \frac{1}{|\Omega|}\sum_{\mathbf{r}'\in\Omega(\mathbf{r})} e^{i\gamma\cdot T_E\cdot b(\mathbf{r}',t)} \text{ (intravoxel dephasing mechansim)} \\ &\triangleq A[\mathbf{r},t]e^{i\Phi[\mathbf{r},t]} \quad \text{(complex in \{magnitude, phase\}format)} \end{aligned} \tag{5}$$

where γ denotes the proton gyromagnetic ratio (a constant), $\Omega(\mathbf{r})$ a small voxel at $\mathbf{r} = (x,y,z)$, $|\Omega(\mathbf{r})|$ the voxel size (in a measure of a number of proton spins in a voxel space),and $1/|\Omega|$ for signal normalization ($C[\mathrm{T_E} = 0] = 1$). The intravoxel dephasing signal formation implements a data mapping from a real-valued continuous fieldmap $b(\mathbf{r},t)$ to a complex-valued discrete T2* image $C[\mathbf{r},t]$, where $(\mathbf{r},t)$ denotes the continuous space and time variables and $[\mathbf{r},t]$ their discrete versions. The T2* imaging is a continuous-to-discrete non-linear data transformation,

which denies a closed form for an explicit analytic expression for the voxel magnitude and phase signals (the discrete $A[\mathbf{r},t]$ and $P[\mathbf{r},t]$) in relation to the continuous fieldmap $b(\mathbf{r},t)$.

The nonlinearity of $A[\mathbf{r},t]$ can be illustrated with its 1st-order approximations (reported in Appendix B3) by

$$A[\mathbf{r},t] \approx 1+\frac{(\gamma T_E)^2}{2|\Omega|}\sum_{\mathbf{r}'\in\Omega(\mathbf{r})}(b(\mathbf{r}',t))^2 \ (1^{st}-\text{order approx.}) \tag{6}$$

That is, the T2* magnitude assumes a quadratic nonlinearity under the 1st–order approximation. Therefore, we conclude that the T2* magnitude is an inherent nonlinear transformation of the fieldmap, which disables an inverse solution due to an irreversible nonlinearity like $|\pm a| = a \geq 0$ (the least nonlinear condition of the 1st–order approximation in Appendix A2 and B3). In practice, the magnitude loss (calculated by 1—$A[\mathbf{r},t]$), which represents a non-decay signal by 0), is used in fMRI instead.

Meanwhile, with 1st- and 2nd-order T2* phase signal approximations (reported in Appendix B4) and fieldmap perturbation model (in Eq (4)), we illustrate the $P[\mathbf{r},t]$ nonlinearity and its perturbation decomposition by

$$\begin{aligned} P[\mathbf{r},t] &\approx \arctan\left(\frac{\gamma T_E b[\mathbf{r},t]}{1-(\gamma T_E)^2 b^2[\mathbf{r},t]/2}\right) && (2^{\text{nd}}-\text{order approx.}) \\ &\approx \gamma T_E b[\mathbf{r},t] && (1^{st}-\text{order approx.}) \\ &= P_0[\mathbf{r}]+\delta\Phi[\mathbf{r},t] && (\text{phase perturbation}) \end{aligned}$$

$$\begin{aligned} &\text{with } P_0[\mathbf{r}] = \gamma T_E b_0[\mathbf{r}], \qquad \delta P[\mathbf{r},t] = \gamma T_E \delta b[\mathbf{r},t] \\ &b_0[\mathbf{r}] = \frac{1}{|\Omega|}\sum_{\mathbf{r}'\in\Omega(\mathbf{r})} b_0(\mathbf{r}'), \qquad \delta b[\mathbf{r},t] = \frac{1}{|\Omega|}\sum_{\mathbf{r}'\in\Omega(\mathbf{r})}\delta b(\mathbf{r}',t) \\ &b[\mathbf{r}] = \frac{1}{|\Omega|}\sum_{\mathbf{r}'\in\Omega(\mathbf{r})} b(\mathbf{r}'), \qquad b^2[\mathbf{r},t] = \frac{1}{|\Omega|}\sum_{\mathbf{r}'\in\Omega(\mathbf{r})} b^2(\mathbf{r}',t) \end{aligned} \tag{7}$$

It is shown that the T2* phase signal is nonlinearly related to the fieldmap in a general setting. The linear approximation (see Appendix) leads to a linear mapping between $b[\mathbf{r},t]$ and $P[\mathbf{r},t]$, and the BOLD perturbation modeling (in terms of $\chi = \chi_0 + \delta\chi$ and $b = b_0 + \delta b$) leads to a phase perturbation decomposition ($P = P_0 + \delta P$).

Inverse fMRI

In the context of medical imaging, the source can be reproduced by seeking an inverse imaging solution. As indicated in Eq (6), the T2* magnitude imaging is irreversible, implying that the χ source cannot be reconstructed from T2* magnitude images. Fortunately, we can perform an inverse solution to the linear T2* phase imaging model in Eq (7). In corresponding to two forward mappings ($\chi(\mathbf{r},t) \rightarrow b(\mathbf{r},t) \rightarrow P[\mathbf{r},t]$), we perform two inverse mappings ($P[\mathbf{r},t] \rightarrow b[\mathbf{r},t] \rightarrow \chi[\mathbf{r},t]$) by a computed inverse MRI (CIMRI) model [20]. The BOLD perturbation model offers a two-step forward mapping $\delta\chi(\mathbf{r},t) \rightarrow \delta b(\mathbf{r},t) \rightarrow \delta P[\mathbf{r},t]$ for a continuous-to-discrete conversion and a two-step inverse mapping $\delta P(\mathbf{r},t) \rightarrow \delta b[\mathbf{r},t] \rightarrow \delta\chi[\mathbf{r},t]$ for a discrete source reproduction.

Brain χ[r,t] source reconstruction

A raw T2* phase image is usually severely wrapped, especially for high-field T2* phase imaging. The phase wrapping phenomenon can be removed through the use of a phase unwrapping algorithm. There have been many reports on 3D MRI phase unwrapping. Perhaps the most efficient 3D phase unwrapping can be achieved by a Laplacian technique [27,28], which has been used for brain phase image processing [16,29]. Applied to a 3D wrapped phase image $P^{wrap}(\mathbf{r}) \in [-\pi, \pi)$ rad, the Laplacian unwrapping algorithm is expressed [16,29] by

$$P^{unwrap} = FT^{-1}\left\{\frac{FT\left\{\cos P^{wrap} \cdot FT^{-1}\left(k^2 \cdot FT(\sin P^{wrap})\right) - \sin P^{wrap} \cdot FT^{-1}\left(k^2 \cdot FT(\cos P^{wrap})\right)\right\}}{k^2}\right\} \text{(unwrapping)} \quad (8)$$

with $P^{\text{wrap}} \in [-\pi, \pi)$ and $P^{unwrap} \in (-\infty, \infty)$

where FT and FT^{-1} is a Fourier transform pair (with an identity $FT^{-1}(FT) = 1$) and $k = |\mathbf{k}|$ represents the 3D discrete coordinates in the 3D Fourier domain. Besides phase unwrapping, the Laplacian algorithm in Eq (8) can largely remove the harmonic background phase [16,29] (in principle of $\nabla^2 e^{iP(\mathbf{r})} = 0$). By applying a 3D Laplacian unwrapping procedure to each 3D phase image in $P^{wrap}[\mathbf{r},t]$ at a time point t, we obtain a 4D unwrapped phase dataset $P^{unwrap}[\mathbf{r},t] \in (-\infty,\infty)$ rad.

With the linear T2* phase imaging model in Eq (7), from an unwrapped phase image (denoted by *P for succinct*), we can reconstruct the fieldmap by

$$b[\mathbf{r}, t] = \frac{P[\mathbf{r}, t]}{\gamma T_E} \text{ (linear T2} * \text{ phase imaging)}. \quad (9)$$

It is noted that $b[\mathbf{r},t]$ and $P[\mathbf{r},t]$ are spatially conformed to the scale difference $(1/(\gamma T_E))$ at each snapshot time *t*. The linear inverse mapping from $P[\mathbf{r},t]$ and $b[\mathbf{r},t]$ cancels the T_E parameter dependence.

Using the $b[\mathbf{r},t]$ dataset, we can then reconstruct a $\chi[\mathbf{r},t]$ dataset by solving a dipole inversion problem. An iterative solution is given by

$$\chi[\mathbf{r}, t] = \arg\min_{\chi[\mathbf{r},t]} \left(B_0 \chi[\mathbf{r}, t] * h_{dipole}[\mathbf{r}] - b[\mathbf{r}, t]\right). \quad (10)$$

where the reconstructed 4D $\chi[\mathbf{r},t]$ provides a discrete representation of the continuous brain dynamic source $\chi(\mathbf{r},t)$, hence the 4D χ tomography [30,31]. It is noted that the parameter B_0 is canceled and the spatial convolution is removed in Eq (10). The discreteness effect associated with the computationally tomographic χ reconstruction diminishes as the spatial resolution increases.

The solution to the iterative dipole inversion problem is a nontrivial task. We refer readers to different solutions, such as truncated inverse filtering (filter truncation regularization) [32,33], iterative L_1-norm or L_2-norm regularizations [34–38], and total-variation (TV)-regularized split Bregman iteration (TVB) [20,30,34,39,40].

BOLD δχ source reconstruction

From a 4D T2* phase dataset, we can extract the dynamic relative phase change (relative to a reference or baseline) by a complex division algorithm [8]:

$$\delta P[\mathbf{r}, t_n] = Arg\left(\frac{\exp(iP[\mathbf{r}, t_n])}{\exp(iP_{ref}[\mathbf{r}])}\right), n = [1, 2, \cdots, N_t] \quad (11)$$
$$with\ P_{ref}[\mathbf{r}] = P[\mathbf{r}, t_1]$$

where *Arg* denotes an operator to find the phase angle (or argument) of a complex number (via a trigonometric function *arctan*) and N_t is the number of snapshot captures in a 4D T2* dataset. The reference phase image $P_{ref}[\mathbf{r}]$ is selected from a T2* phase image captured at a time point (not necessarily the 1st time point). The complex division serves as a phase subtraction algorithm to find the phase difference between two phase images. Notably, it can correctly extract the relative phase change $\delta P[\mathbf{r},t]$ between two wrapped phase images as long as $|\delta P| < \pi$. For a timeseries of severely wrapped T2* phase images, we can extract the temporal phase changes (relative to a snapshot reference) using the complex division in Eq (11), obtaining a 4D dataset $\delta P[\mathbf{r},t]$ in which each 3D δP map is free from phase wrapping phenomenon ($|\delta P| < \pi$). In this sense, the complex division algorithm implements phase unwrapping in the time domain [8,9]. Obviously, the static phase background $P_0(\mathbf{r})$ (the culprit of phase wrapping effect) is completely removed by the complex division in Eq (11).

From the 4D dataset $\delta P[\mathbf{r},t]$, we can reconstruct a 4D dataset $\delta\chi[\mathbf{r},t]$ in the same manner as for 4D $\chi[\mathbf{r},t]$ reconstruction, as represented by

$$\delta\chi^{recon}[\mathbf{r},t] = \arg\min_{\delta\chi[\mathbf{r},t]} \left(B_0 \delta\chi[\mathbf{r},t] * h_{dipole}[\mathbf{r}] - \frac{1}{\gamma T_E} \delta P[\mathbf{r},t] \right) \tag{12}$$

Again, the MRI parameters $\{B_0, T_E\}$ are cancelled and the dipole effect is removed in the iterative minimization solution.

Brain function map extraction

As discussed above, a brain activity may be represented in a variety of timeseries images from different perspectives, such as in T2* image dataspaces by {'$A[\mathbf{r},t]$', '$P[\mathbf{r},t]$', '$\delta P[\mathbf{r},t]$'} and in source dataspaces by {'$\chi[\mathbf{r},t]$', '$\delta\chi[\mathbf{r},t]$'}. Since the BOLD response is very weak (< 5%), a measurement repetition through a designed paradigm is needed for fMRI data acquisition and a statistic parametric mapping (SPM) technique is need for brain function map (*fmap*) extraction. In particular, we are interested in the brain functional mappings in the magnitude image dataspace ($A[\mathbf{r},t]$) and the reconstructed BOLD magnetic source dataspaces ($\chi[\mathbf{r},t]$ and $\delta\chi[\mathbf{r},t]$).

For a 4D dataset from a task-evoked BOLD fMRI study, which acquires a 4D fMRI dataset through a designed task paradigm with a timecourse of *task*[t], we can extract the task-stimulated *fmap* by a task-correlation algorithm [16,18], as given by

$$\begin{aligned} \Lambda_{tcorr}[\mathbf{r}] \quad &= tcorr(\Lambda[\mathbf{r},t], task^*[t]), \text{ for } \Lambda = \{'A', '\chi', '\delta\chi'\} \\ &\text{with } task^*[t] = task[t] * hrf[t] \end{aligned} \tag{13}$$

where *tcorr* stands for temporal correlation, which reduces the 4D spatiotemporal dataset into a 3D spatial map, and *hrf*[t] for a canonical hemodynamic response function (available in SPM software), which accounts for the lagging neurovascular response in response to a task stimulus. The 3D *tcorr* map offers an intuitive understanding of brain function pattern: a large positive *tcorr* represents a high correlative response, while a negative *tcorr* constitutes an anti-correlation response. It is pointed out that the temporal correlation data analysis on a 4D BOLD dataset can largely suppress the effect of physiological fluctuations (e.g., heartbeat and breathing cycles) as long as the task paradigm (a long timecourse of task waveform) is out of the phase with the physiological pulsations.

Signal-to-noise ratio (SNR) and contrast-to-noise ratio (CNR)

A task-evoked BOLD fMRI experiment is essentially a time-locked weak signal repetition detection technique. Through the use of complex division, we can extract the pure BOLD

responses, which are buried in heavy noise. In the experiment result report below, we provided signal-to-noise ratio (SNR) and contrast-to-noise ratio (CNR) measurements to numerically characterize the pure BOLD responses at different stages (in the original source $\delta\chi$, the $\delta\chi$-induced fieldmap δb, and the output image δP). Based on the SNR and CNR definitions reported in [41], we define the dynamic SNR and CNR metrics for a timeseries of images by

$$\begin{aligned} SNR[t] &= \frac{|mean(ROI_{act}[t])|}{std(ROI_{inact}[t])} \\ CNR[t] &= \frac{|mean(ROI_{act}[t]) - mean(ROI_{inact}[t])|}{std(ROI_{inact}[t])} \end{aligned} \tag{14}$$

where $mean(\cdot)$ and $std(\cdot)$ stand for statistic mean and standard deviation, $ROI_{act}[t]$ and $ROI_{inact}[t]$ for activation and inactivation regions of interest at a time point t. The ROI_{act} and ROI_{inact} can be retrospectively specified (through a visual selection of an activation blob and an inactive region in an *fmap* afterward). It is mentioned that the signal noise measurement at an air region (defined in [41]) is applicable for phase signal noise measurement because there is no water proton (signal carrier) in an air region that consequently causes capricious phase signals therein. Instead, we define an inactive tissue region (retrospectively specified) for noise measurement.

Function/structure co-localization

Conventionally, brain anatomical structure is procured by a high-resolution T1 scan (at sub-millimeter resolution). The *fmap* is always displayed over a high-resolution T1 image, which can be obtained by T1 imaging on the same brain (intra-subject inter-scan data acquisition) or adopted from a standard brain template (inter-subject data). The function/structure association requires intra-subject image coregistration that is computationally intensive and prone to digital errors; and additionally, the inter-subject function/structure association suffers from a loss of the brain tissue structure individuality.

Upon availability of high-resolution GRE-EPI data and subsequent high-resolution χ source reconstruction, we propose to co-localize an *fmap* on a brain χ structure background. Since all the data (including raw data and processed data) are derived from the same source at a single scan (intra-scan data derivations), they are spatially automatically coregistrated. High field fMRI enables high-resolution functional mapping and function/structure association with rich spatial information, especially for hopefully scrutinizing the vascular origin of brain function source.

Task fMRI experiments

We conducted one high-field high-resolution task fMRI experiment at the Auburn University MRI Research Center on a healthy adult volunteer. The human subject MRI scanning was approved by the Institutional Review Board at the Auburn University. Written consent was obtained from the human subject before the MRI scanning. The subject was instructed to perform a finger-tapping task using the scan session. The scanner was Siemens MAGNETOM 7T scanner and we used a standard GRE-EPI sequence with the following parameter settings: T_R/T_E = 3000/29 ms, flip angle = 70˚, slice spacing = 0mm, slice oblique = 0˚, voxel size = 0.5 × 0.5 × 1.2 mm^3, and matrix = 234 × 234 × 24 voxels for a coverage of the superior-most portion of the brain encompassing the motor cortex (slab thickness = 28.8mm). These complex images were reconstructed from 32 coil elements through a GRAPPA PAT mode with an acceleration factor of 3 in the phase-encoding dimension and a sum-of-square

algorithm for coil combination (which is optimal for magnitude MRI but suboptimal for phase MRI, leaving a room for improvement). The task consisted of 15-second blocks alternating between task and rest for a total of 50 volumes (5 cycles of {5 ON, 5 OFF}). An in-house modification to the acquisition protocol allowed for the production of both 4D raw magnitude and 4D phase datasets as denoted by $A[x,y,z,t]$ and $\Phi[x,y,z,t]$, in a matrix form of 234×234×24×50.

We also conducted a low-field low-resolution finger tapping task fMRI experiment by scanning a different healthy adult volunteer in a Siemens 3T TrioTim scanner at the Mind Research Network (MRN). The subject experiment was approved by the Institutional Review Board at MRN and by the informed written consent from the subject. The task paradigm was designed as a block timecourse consisting of 5 cycles of {15 OFF, 15 ON} plus 15 OFF, a total number of 165 timepoints. With the experiment settings {standard GRE-EPI sequence, T_R/T_E = 3000/29ms, flip angle = 75°, isotropic voxel = $2 \times 2 \times 2$ mm^3, matrix = 128 ×128×30 voxels for a brain superior coverage}, we obtained a pair of 4D magnitude and phase images in a matrix form of 128 ×128 ×30 ×165.

Results

In this section, we report our experimental results by applying our BOLD perturbation model to two single-subject task fMRI data analyses (data acquisition method was described in the previous section). We applied our perturbation model to these two task fMRI datasets separately by performing forward fMRI phase perturbation decomposition and inverse mapping through the same procedure. We reported the high-resolution 7T task fMRI experimental results in Figs 2 through 6 in technical detail, while summarized the low-resolution 3T task fMRI experimental results in Fig 7.

In Fig 2(a1, b1) we showed a pair of the 7T fMRI magnitude and phase images (raw data) acquired at a snapshot of task-ON state (defined by task*[t] $\geq$ 0.5), and in Fig 2(a2, b2) for the 3D images at a task-OFF state (defined by task*[t] $\geq$ 0.5). The task paradigm for capturing 50 snapshot images is also displayed in Fig 2, in which the waveform task*[t] accounts for the lagging hemodynamic responses. More slices (16 axial slices selected from a 24-slice volume) in a snapshot volume were presented in S1 and S2 Figs. It is noted that the raw T2* phase images are severely phase wrapped in the data range of [-π, -π) rad, and that the differences between a task-ON and task-OFF state (either in magnitude images (a1,a2) or in phase images (b1,b2)) are too subtle to be visually perceived.

In Fig 3(a1, b2) we illustrated the 7T fMRI phase image processing (using Eq (8)) and the $\chi[\mathbf{r},t]$ reconstruction (using Eq (10)), displayed with an axial slice (at z_0 = 10.8 mm distant from brain top). The SNR and CNR values were calculated from the 3D images according to the definition in Eq (14), with the ROI_{act} and ROI_{inact} (in size of 5 × 5 × 3 voxels) retrospectively defined in Fig 5(c2). The task*[t] was included for observing the dynamics of SNR and CNR with respect to the stimuli. The SNR and CNR numbers denote the time averages (over N_t -1 = 49 timepoints). More z-slices of the reconstructed $\chi[\mathbf{r},t]$ (at one time point t_1) were presented in S3 Fig.

From the phase perturbation dataset $\delta P[r,t]$ (obtained by the complex division in Eq (11)), we reconstructed the pure BOLD χ response dataset $\delta\chi[\mathbf{r},t]$ using the TVB algorithm (in Eq (12)), as demonstrated in Fig 4. More z-slices of reconstructed $\delta\chi[\mathbf{r},t]$ (at one time point t_1) were presented in S4 Fig. Note that the task-evoked small BOLD response (in terms of δP or $\delta\chi$) was not visually discernible in a snapshot image in Fig 4.

In Fig 4, we also provided the SNR and CNR measurements for $\delta P[\mathbf{r},t]$ and $\delta\chi[\mathbf{r},t]$ datasets (calculated by Eq (14) with ROI_{act} and ROI_{inact} defined in Fig 5(c2)). We observe the following

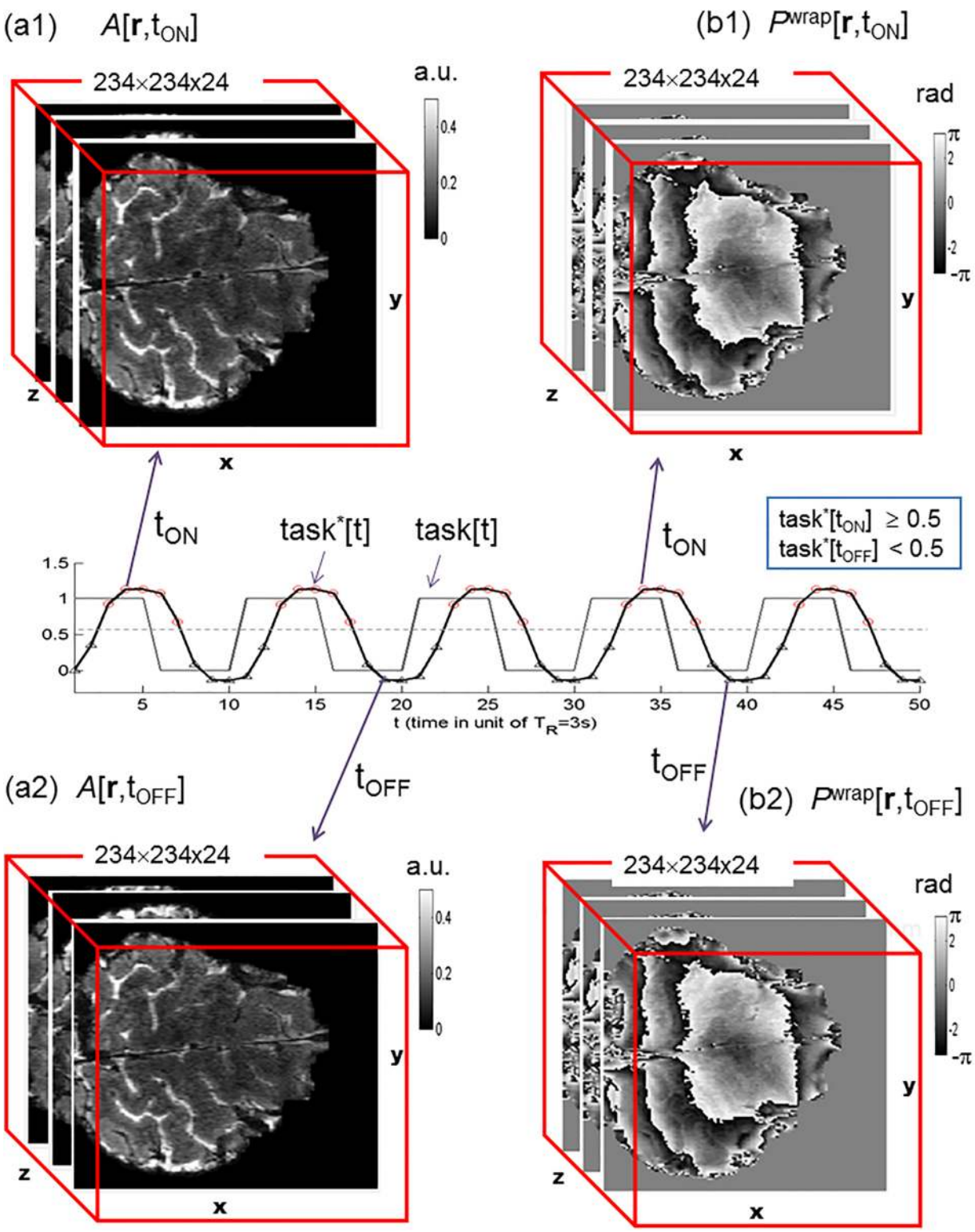

Fig 2. T2* magnitude and phase image acquisition under a task paradigm. The ON states are defined by task*[t] ≥ 0.5 and the OFF states by task*[t] < 0.5.

https://doi.org/10.1371/journal.pone.0191266.g002

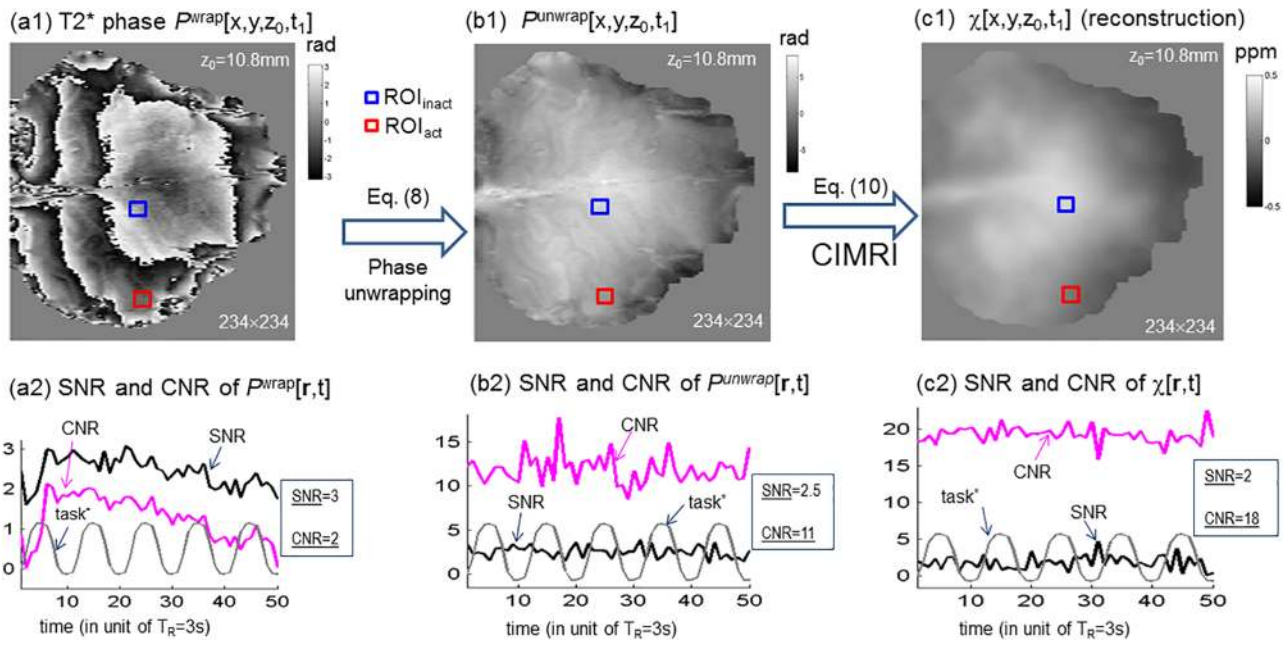

Fig 3. (a1,b1,c1) T2* phase processing and χ[r,t] reconstruction; (a2,b2,c2) SNR and CNR characterizations. The SNR CNR values were calculated according to the definition in Eq (14), with the ROI_{act} and ROI_{inact} defined retrospectively in Fig 5(c2), in a small size of 5 × 5 × 3 voxels. The task* is included to observe the dynamics of SNR and CNR with respect to the stimuli. The SNR and CNR denote time averages.

https://doi.org/10.1371/journal.pone.0191266.g003

aspects: i) the reconstructed χ[**r**,t] and δχ[**r**,t] assume different value ranges: χ∈[-0.5, 0.5] ppm (part per million, 10^{-6}, in SI metric) and χ∈[-0.03, 0.03] ppm, indicating the weakness of the BOLD perturbation δχ; ii) The spatial maps of χ[**r**,t] and δχ[**r**,t] are more spatially smoothed than those of P[**r**,t] and δP[**r**,t] due to the removal of the spatial derivative property of dipole effect (5); and iii) The dataset δχ[**r**,t] gains higher SNR and CNR values than the dataset δ*P*[**r**,t] does (specifically, $SNR_{\delta\chi}$ = 8.5 and $CNR_{\delta\chi}$ = 5.2 versus $SNR_{\delta P}$ = 0.31 and $CNR_{\delta\chi}$ = 0.34).

From 4D datasets {*A*[**r**,t], χ[**r**,t] and δχ[**r**,t]} (displayed with a z-slice in Fig 5(a1,b1,c1)), we extracted the task-evoked brain *fmaps* using Eq (13), and obtained the 3D *fmaps* {A_{tcorr}[**r**], χ_{tcorr}[**r**], $\delta\chi_{tcorr}$[**r**]} as displayed in Fig 5(a2,b2,c2). With inspection, we could identify the brain active blobs at the motor cortex. We define an active and inactive region of interest (denoted by ROI_{act} and ROI_{inact}, in size of 5 × 5× 3 voxels, corresponding to 2.5 × 2.5 × 3.6 mm^3) for image SNR and CNR calculations (in Eq (14)). In (a3,b3,c3), we also provide the p-values for the *tcorr* calculations, which reveals an edge effect of *tcorr*-based *fmap* extractions in the reconstructed source dataspaces (in the χ_{tcorr} and $\delta\chi_{tcorr}$ maps). Specifically, the maximal *tcorr* was calculated at the activation foci (inside the blob in the ROI_{act}) with a very small p-value ($< 10^{-2}$ for $\delta\chi_{tcorr}$ in Fig 5(c3)), implying a high statistical stability for the correlation-based task idenfication. It is noted in Fig 5 that the task functional mapping using the reconstructed χ data (b1,b2,b3) is less statistically reliable than using the reconstructed δχ data (c1,c2,c3) (as inferred from the p-value maps (b2) and (c2)). The montage displays for the 3D *tcorr fmaps* are presented in S5, S6 and S7 Figs.

Finally, we need to visualize the function/structure association. Instead of adopting a brain anatomical template, we used a brain structure image (denoted by χ_0[**r**]) for *fmap* visualization by selecting a 3D χ source volume from χ[**r**,t]. We performed image enhancement (e.g., a homodyne filtering [42]) on χ_0[**r**] to enhance the cortex structure (gyri and sulci patterns). The montage displays of 3D image χ_0[**r**] are presented in S8 Fig. At the 0.5 mm in-plane spatial

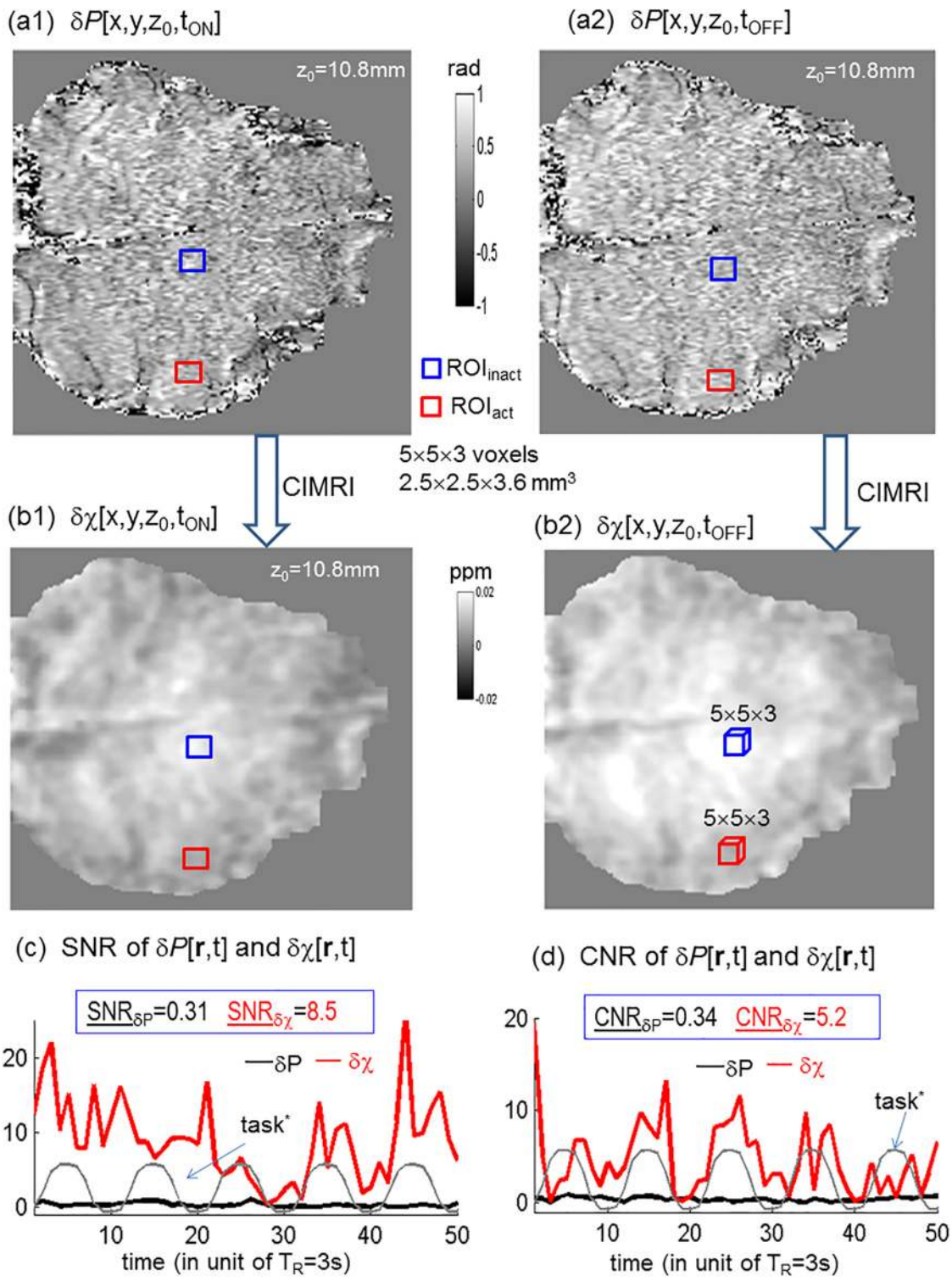

Fig 4. The BOLD δχ[r,t] reconstruction from δ*P*[r,t] by CIMRI (demonstrated with a z_0 slice in a volume at an ON and OFF snapshot). The SNR and CNR values were calculated according to the definition in Eq (14), with the ROI_{act} and ROI_{inact} defined retrospectively in Fig 5(c2), in a small size of 5 × 5 × 3 voxels. The SNR and CNR denote time averages. The task* is included to observe the dynamics of SNR and CNR with respect to the stimuli. The ON and OFF snapshots are labeled in Fig 2.

https://doi.org/10.1371/journal.pone.0191266.g004

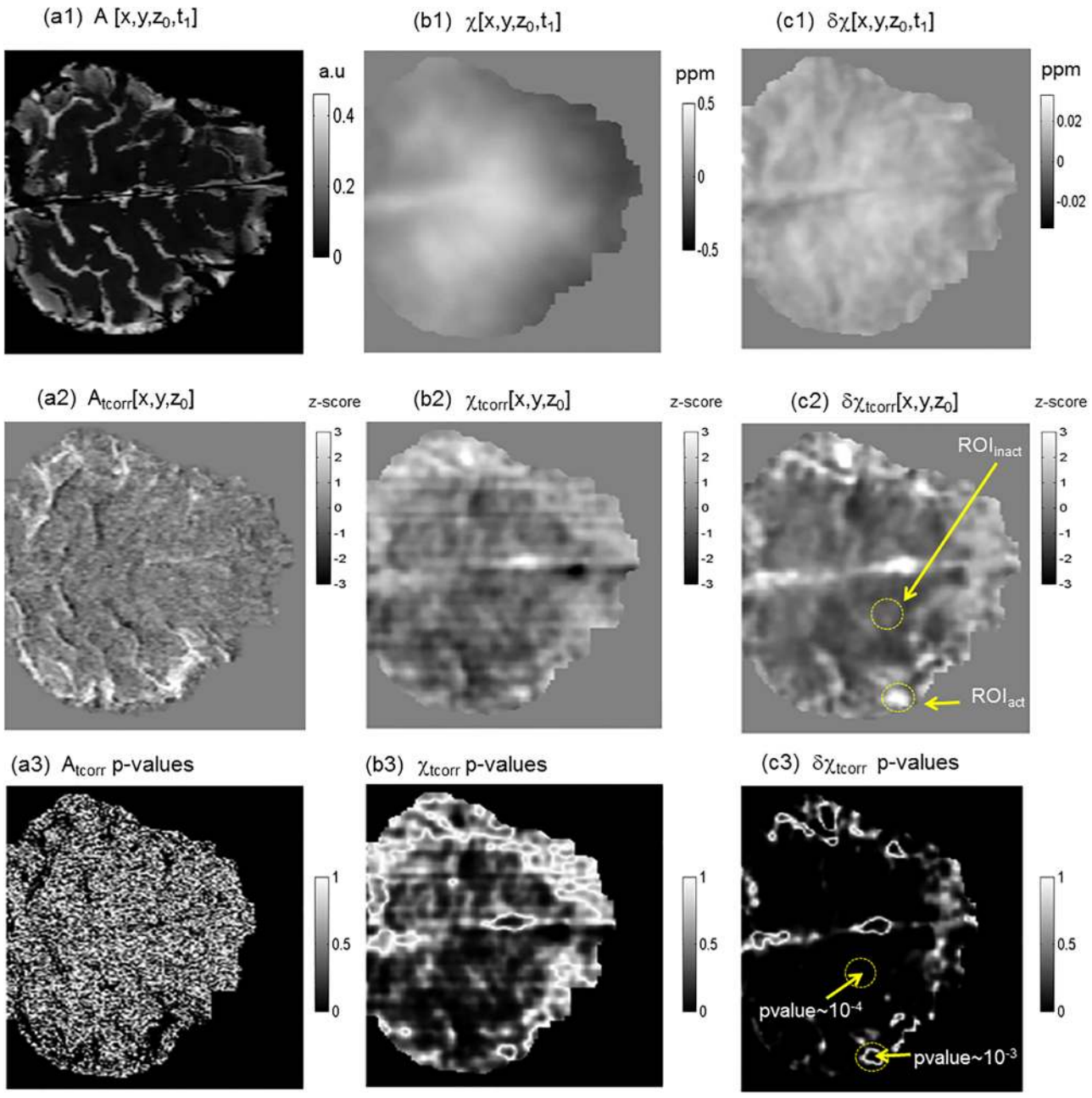

Fig 5. Task-evoked brain functional mappings in different dataspaces: (a1, a2, a3) T2* magnitude image dataspace *A*[r,t]; (b1,b2,b3) the reconstructed χ[r,t] source dataspace (including static background); (c1,c2,c3) the reconstructed δχ[r,t] source dataspace (pure BOLD χ responses). In (c2), the ROI_{act} defines a task-evoked active region of interest, and the ROI_{inact} defines a task-irrelevant region of interest.

https://doi.org/10.1371/journal.pone.0191266.g005

resolution, the reconstructed χ_0 images reveal superior sagittal sinus and cortical details (gyri and sulci patterns), but the intra-cortex vasculature remains undiscernible.

In Fig 6, we visually compare the magnitude-depicted *fmap* $A_{tcorr}[\mathbf{r}]$ and the δχ-depicted *fmap* $\delta\chi_{tcorr}[\mathbf{r}]$ by color displays in (a1,a2), thresholded blob displays on reconstructed χ structure background in (a2,b2), and magnified blob displays in the insets. It is observed that the $\delta\chi_{tcorr}[\mathbf{r}]$ *fmap* reveals bidirectional BOLD χ responses to the task stimuli with compact and

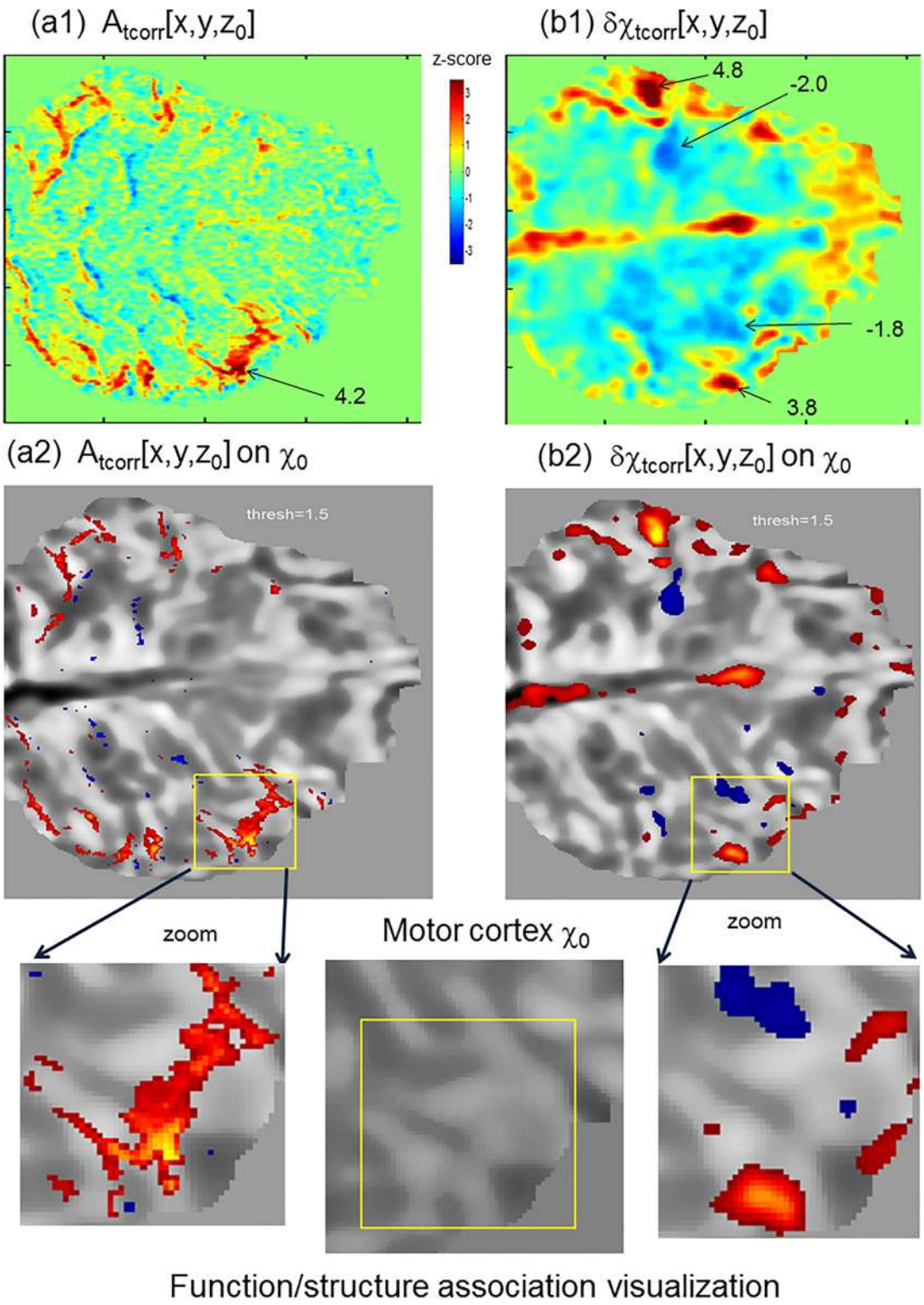

Fig 6. Visualization of magnitude- and susceptibility-depicted brain *fmaps* (on the reconstructed χ motor cortex image). (a1,a2) Magnitude-based *fmap* (A_{tcorr}); (b1, b2) BOLD χ-depicted *fmap* ($\delta\chi_{tcorr}$). The magnified insets are for scrutinizing function/structure associations. The numbers in (a1,a2) denote the z-scored *tcorr* values at the activation blobs.

https://doi.org/10.1371/journal.pone.0191266.g006

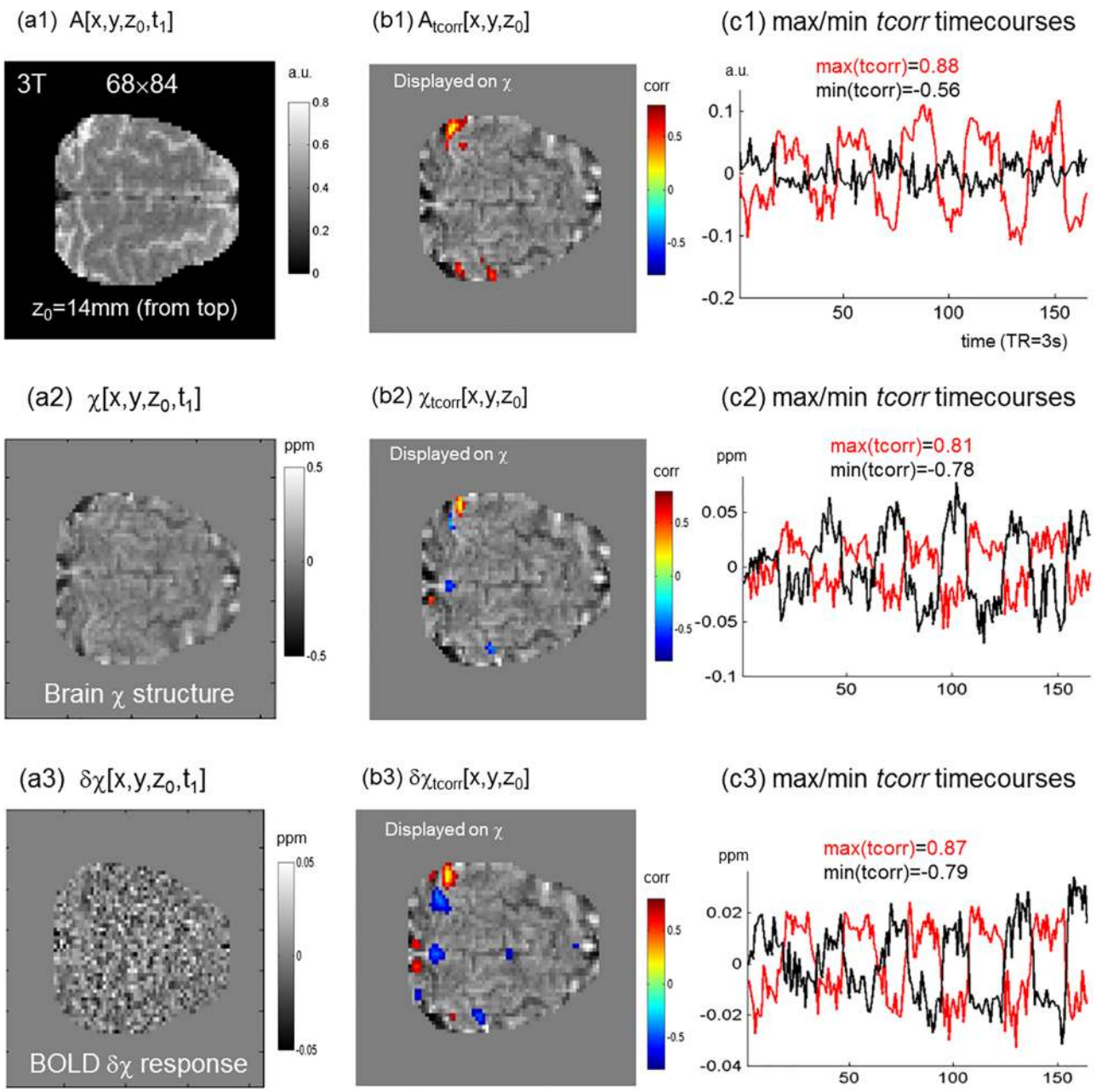

Fig 7. A low-field (3T) and low-resolution (2mm) brain task fMRI experiment (finger tapping) with task function analyses in different dataspaces: (a1,b1,c1) fMRI magnitude, (a2,b2,c2) reconstructed susceptibility (χ), and (a3,b3,c3) reconstructed temporal susceptibility change (δχ). A brain snapshot state (at a timepoint t_1) was displayed with an axial slice (z_0 = 14mm from brain top) in (a1) magnitude, (a2) reconstructed χ, and (a3) reconstructed δχ. Correspondingly, task correlation *fmap*'s were displayed in (b1,b2,b3); and the maximal (red) and minimal (black) task-correlated voxel timecourses were plotted in (c1,c2,c3). Note that the functional *tcorr* maps (b1,b2,b3) were displayed over the reconstructed brain χ image (a2). Display units: *a.u.*, arbitrary unit (dimensionless); *corr*, correlation value in range [−1, 1] (dimensionless); *ppm*, parts per million 10^{-6} (dimensionless).

https://doi.org/10.1371/journal.pone.0191266.g007

strong activation blobs. In comparison, the conventional $A_{\text{tcorr}}[\mathbf{r}]$ *fmap* appears a positive dominance with more spatially spread in response patterns. Since all the images were derived from the same scan data (intra-scan data), they were automatically self-aligned, thus facilitating the function/structure associations.

In Fig 7, we showed the low-resolution (2mm) 3T task fMRI data analysis results. In the top row (a1,b1,c1), we displayed the task functional mapping in terms of the brain structural image (in an axial slice), the task-evoked *fmap* (in an axial slice) and the most positive and negative responsive timecourses (at one activation focus with *max*(*tcorr*) for task correlation and at another activation focus with a negative *min*(*tcorr*) for task anticorrelation). In the middle row (a2,b2,c2) were showed the task functional mapping using the reconstructed full χ data (BOLD response was superimposed on the background); and in the bottom row (a3,b3,c3) were showed the pure BOLD response using the reconstructed $\delta\chi$ data by excluding the static background.

The 3T experimental results in Fig 7 reveal the following aspects: 1) The pure BOLD $\delta\chi$ response was too weak and noisy to be observable in a single snapshot (in Fig 7(a3)) and the task map was extracted through a timeseries of 165 snapshots; 2) The reconstructed $\delta\chi$ data yielded a higher task extraction performance than the reconstructed full χ data (in terms of *max*(*tcorr*) in (c2,c3)); 3) The $\delta\chi$-depicted task activation patterns consists of spatially separated positive and negative blobs (bidirectional responses), which is different from the magnitude-depicted the prevailing positive response (cf. (b1, b3)); and 4) The low-resolution (2mm) χ image (a2) hinders the cortical details (gyri and sulci) for the function/structure co-localization in comparison with the high-resolution (0.5mm) χ image (the background image in Fig 6(b2)). Overall, this 3T task fMRI experiment shows that our BOLD perturbation model is also applicable to low-resolution low-field individual fMRI data analysis.

Discussion

Under linear approximations of T2* phase imaging and with the additive BOLD perturbation model, we can trace the BOLD activity (in a perturbation term) at different imaging stages. Specifically, BOLD activity is expressed by $\delta\chi$ in the original source (with a $\chi + \delta\chi$ model), δb in the fieldmap ($b + \delta b$ model), and δP in the T2* phase image ($P + \delta P$ model). Reversely, the BOLD signal decomposition enables inverse mappings of pure BOLD responses in the magnetic source dataspace by solving an inverse fMRI problem while excluding the static non-BOLD signals.

In our previous publications [5,16,20,39], we have reported on a two-step forward mapping model for brain MRI and a corresponding two-step inverse mapping model (a linear CIMRI model [20]) that is for χ source reconstruction (called χ tomography in the context of source reconstruction in medical imaging [16,30,31]). We apply the two-step inverse mapping model for brain full χ source reconstruction, as illustrated by a data flow $P[\mathbf{r},t] \rightarrow b[\mathbf{r},t] \rightarrow \chi[\mathbf{r},t]$. With the BOLD perturbation model, we are allowed to trace the data transformations on a BOLD signal during BOLD fMRI data acquisition, as illustrated by $\delta\chi(\mathbf{r},t) \rightarrow \delta b(\mathbf{r},t) \rightarrow \delta P[\mathbf{r},t]$. Correspondingly, by rendering inverse mappings, as denoted by $\delta P[\mathbf{r},t] \rightarrow \delta b[\mathbf{r},t] \rightarrow \delta\chi[\mathbf{r},t]$, we reproduce the original intrinsic pure BOLD magnetic responses. Both χ and $\delta\chi$ reconstructions are implemented by CIMRI, which is essentially a linear inverse imaging solution.

The reconstruction of 4D $\chi[\mathbf{r},t]$ dataset from a 4D $P[\mathbf{r},t]$ dataset (unwrapped phase images) is essentially a repetition of quantitative susceptibility mapping (QSM) [34–38] at a timeseries of snapshot images. There is an emergence of brain functional mapping in the reconstructed magnetic susceptibility source data space, as termed by functional χ mapping [16] or functional QSM [43,44], for more direct sourced-based brain function depiction. In fact, the QSM was demonstrated in Fig 3 with a signal snapshot volume reconstruction. In the framework of QSM, one difficulty is to unwrap the severely wrapped phase images and remove the phase background, which can be effectively and efficiently solved through the use of Laplacian unwrapping technique [27,28] (in Eq (8)). Fortunately, the 4D $\delta\chi[\mathbf{r},t]$ reconstruction does not

involve the awkward phase unwrapping and phase background removal at all. The other difficulty is a 3D dipole inversion, which is afflicted by a "divide-by-zero" problem, for which we approach through a TVB iteration technique by dealing with a "multiply-by-zero" problem instead [20,30,34,39,40].

A BOLD activity map can be extracted from a timeseries of T2* magnitude images through the use of SPM (http://www.fil.ion.ucl.ac.uk/spm/), which is a software tool for whole brain functional mapping. In our high-field high-resolution experiment by a GRE-EPI sequence, we could cover a chunk of brain superior portion (with a thickness of 28.8mm from brain top), which is not suitable for whole brain functional mapping by SPM. Expediently, we presented the *tcorr* maps for functional mappings.

Our previous reports [5,17] show that the magnitude-based brain fMRI suffers from nonlinear distortional mappings. With the BOLD perturbation model, we herein show that there is a nonlinear interaction between the dynamic BOLD perturbation and the static background in a T2* magnitude signal that manifests as a quadratic nonlinearity under the 1st order Taylor expansion (in Appendix). This implies that a BOLD activity cannot be separated from the non-BOLD background in a T2* magnitude signal. A high field (or a long T_E) aggravates the nonlinear magnitude signal coupling due to more nonlinear terms introduced from high-order Taylor expansions. This poses a caveat on the magnitude-based brain fMRI and neuroimaging from the viewpoint of inseparable magnitude signals[17]. In comparison, we can derive a linear T2* phase imaging model from the 1st-order Taylor expansion. It is understandable that higher-order Taylor expansions will bring more phase nonlinearity [7].

The Taylor expansion on a preliminary proton precession signal (in Appendix) is a mathematic manipulation in a small phase angle condition, $|\gamma b T_E| << 1$ rad, which is seldom satisfied in a practical BOLD fMRI experiment. Nevertheless, the Taylor expansion reveals different magnitude and phase nonlinear behaviors [7]. Theoretically, the phase perturbation term δP (extracted by complex division) could better meet the small phase angle condition (see Fig 4(a1,a2) for $|\delta P| < 1$ rad) than the full phase signals (see Fig 5(b1) for $P \in (-6, 6)$ rad). That is, the $\delta\chi$ reconstruction suffers less nonlinearity than the χ reconstruction. It is remind of the displays of $\{P, \delta P, \chi, \delta\chi\}$ in different window levels (grayscales or colorbars). In the sense of depiction accuracy, we advocate brain functional χ mapping in the reconstructed $\delta\chi$ dataspace instead of χ dataspace.

The brain χ source may assume a bipolar-valued distribution in reflection of the brain tissue diamagnetism and paramagnetism. The χ-expressed brain structure reconstruction from a snapshot T2* phase volume is essentially a QSM technique. It is a new concept to represent a brain tissue structure image by a bipolar-valued χ map [45], which is only available by a computational imaging approach that allows negative values. Indeed, there exist both χ-expressed positive and negative brain tissues. Specifically, a reconstructed brain χ image may assume negative values (e.g. $\chi_{water} < 0$) and positive values (e.g. $\chi_{ferritin} > 0$ and $\chi_{myelin} > 0$), and the BOLD $\delta\chi$ perturbation may assume negative values (e.g., $\chi_{oxyHb} < 0$) and positive values (e.g. $\chi_{deoxyHb} > 0$). The linear T2* phase imaging retains the signs of bipolar-valued χ source, whereas the T2* magnitude imaging completely suppresses the signs due to nonnegative mapping. In particular, our experiment reveals concurrent positive and negative BOLD χ responses (see $\delta\chi_{tcorr}$ in Figs 5 and 6), which may indicate the biological antagonism and homeostasis during a brain activity: a stimulus evokes a positive response in one region (excitation) meanwhile a negative response in another region (inhibition). In comparison, the conventional magnitude-depicted *fmap* reveals prevailing positive responses over the brain (see A_{tcorr}).

In this report, we demonstrated our brain functional BOLD perturbation model for task fMRI data analysis through the use of two single-subject task fMRI datasets acquired in

different experiment settings. Both experimental data analyses produced similar results. Since BOLD changes are relatively small, we cannot observe a brain function activity from a snapshot image. Through a designed task paradigm, we can infer the brain activity from a timeseries of repeating measurements through a task correlation method. Specifically, we used a timeseries of 50 snapshots (in 5cylces) in our 7T task fMRI experiment and a longer timeseries of 165 snapshots (in $5\frac{1}{2}$ cycles) in our 3T experiments. Besides the individual fMRI study, the brain functional BOLD perturbation model is in principle applicable to group-level multi-subject brain function analysis. This is an ongoing research topic.

The brain functional BOLD perturbation model is very useful for brain fMRI data analysis and computationally inverse mapping for brain χ source reconstruction. It is also useful for numerical BOLD fMRI simulations [14,46]. In principle, a BOLD fMRI signal is, in general, nonlinearly generated from a magnetic source (primarily χ); consequently, neither the magnitude nor the phase signal is a faithful representation of the internal magnetic source. The BOLD perturbation model includes a linearization strategy: extracting a weak dynamic signal from a static background-dominated nonlinear signal for linear dynamic signal processing. Specifically, we separate a small BOLD response in a part of fMRI phase by complex division and reconstruct the pure BOLD χ response by inverse mapping under linear approximations, thereby avoiding the inherent fMRI nonlinearity [7].

Summary and conclusion

Brain activity only contributes to a very small portion of a brain fMRI signal ($T2^*$ magnitude signal), which has been modeled by a BOLD contrast mechanism. We propose using a BOLD perturbation model for better understanding the BOLD fMRI model from the viewpoint of MRI transformations. The BOLD perturbation model originally represents a neurovascular activity by a small additive perturbation term (δχ) in a magnetic-susceptibility-expressed state (χ), i.e., separating a weak dynamic BOLD activity from an overwhelming static background in the expression of χ source. Under linear approximations of tissue magnetization, the BOLD activity is represented in a δχ-induced fieldmap perturbation (δb). Finally, $T2^*$ imaging conveys a BOLD activity in a complex $T2^*$ dataset. By performing a complex division on the timeseries of $T2^*$ phase images (usually wrapped), we can extract a temporal phase change (relative to a baseline) that is construed as the BOLD phase perturbation (δP). Under linear approximations of $T2^*$ phase imaging, we show in theory that the BOLD perturbation model leads to a cascade of linear mappings: $\delta\chi \rightarrow \delta b \rightarrow \delta P$. By inverse mappings ($\delta P \rightarrow \delta b \rightarrow \delta\chi$), we reconstruct the BOLD δχ source from the BOLD δP image. For the task-evoked BOLD fMRI experiment, we extracted the brain functional activity map from the reconstructed BOLD δχ data in a measure of task correlative response. In this proof-of-concept experiment, we demonstrated the BOLD perturbation model for brain functional data analysis and found the bidirectional brain χ responses in the reconstructed magnetic source dataspace. We also show that high-field high-resolution data enable more informative function and structure depiction, especially the function/structure association visualization with rich cortical details.

In conclusion, we propose a BOLD perturbation model to represent the magnetic source as a dynamic BOLD response imposed on a static background, and thereby trace the components separately in the forward fMRI for data acquisition and the inverse mapping for BOLD χ source reconstruction. The reconstructed pure BOLD χ source (δχ) allows us to look into brain functional activity more directly (i.e., in magnetic χ expression) and more accurately (i.e., basically free from MRI-introduced transformations).

Appendix

A. Taylor expansion of single proton precession signal

A T2* voxel signal is a spatial average of numerous preliminary nuclear proton precession signals in a voxel space. Over a fieldmap $b(\mathbf{r})$, a nuclear proton precession signal is given by $\exp(i\gamma T_E b(\mathbf{r}))$. The 1st and 2nd order Tayler expansions of the complex signal with respect to $b(\mathbf{r})$ are

$$\begin{aligned}
&\exp(i\gamma T_E b)) = \exp(i\gamma T_E b) \\
&= 1 + i\gamma b T_E + \frac{(i\gamma b T_E)^2}{2!} + \frac{(i\gamma b T_E)^3}{3!} + \cdots \\
&\approx 1 + i\gamma b T_E + \frac{(i\gamma b T_E)^2}{2!} \qquad (2^{\text{nd}}-\text{order approx.}) \\
&\approx 1 + i\gamma b T_E \qquad (1^{\text{st}}-\text{order approx.})
\end{aligned} \tag{A1}$$

Specifically, the 1st–order magnitude approximation is

$$\begin{aligned}
a(\mathbf{r}) &\approx \sqrt{1 + (\gamma \cdot b(\mathbf{r}) \cdot T_E)^2} \qquad (\text{1st Taylor expansion}) \\
&\overset{\sqrt{1+x}\approx 1+x/2}{\approx} 1 + (\gamma \cdot b(\mathbf{r}) \cdot T_E)^2/2 \ (\text{s.t.} |\gamma \cdot \delta b(\mathbf{r}) \cdot T_E| << 1)
\end{aligned} \tag{A2}$$

And the 1st-order phase approximation is

$$\begin{aligned}
&p(\mathbf{r}) \approx \arctan(1 + i\gamma b T_E)(1^{\text{st}}\ \text{Taylor expansion}) \\
&= \arctan(\gamma b T_E) \\
&\overset{\arctan x \approx x}{\approx} \gamma b T_E \qquad (\text{s.t.} |\gamma \cdot b \cdot T_E| << 1)
\end{aligned} \tag{A3}$$

It is seen that the preliminary proton spin precession signal is of an inherent trigonometric nonlinearity. Its magnitude signal is of nonlinearity and non-negativity at all circumstances (taking on a quadratic behavior as the least nonlinearity at the 1st–order approximation). Its phase signal reveals linear behavior under linear approximations (resulting from the 1st order Taylor approximation together with a trigonometric approximation: $arctan(x) \approx x$).

B. Approximations of intravoxel dephasing magnitude and phase signals

A complex T2* signal is generated by an intravoxel dephasing average formula in Eq (5). The T2* magnitude and phase signals are calculated by

$$\begin{cases}
A[\mathbf{r}, t] = |C[\mathbf{r}, t]| = \dfrac{1}{|\Omega|} \sqrt{\left(\sum\limits_{\mathbf{r}' \in \Omega} \cos(\gamma b(\mathbf{r}', t) T_E)\right)^2 + \left(\sum\limits_{\mathbf{r}' \in \Omega} \sin(\gamma b(\mathbf{r}', t) T_E)\right)^2} \\
P[\mathbf{r}, t] = \angle C[\mathbf{r}, t] = \arctan\left(\dfrac{\sum\limits_{\mathbf{r}' \in \Omega} \sin(\gamma b(\mathbf{r}', t) T_E)}{\sum\limits_{\mathbf{r}' \in \Omega} \cos(\gamma b(\mathbf{r}', t) T_E)}\right)
\end{cases} \tag{B1}$$

Note the notation [**r**,t] for discrete voxel signals.

Based on the proton precession signal expansions in Appendix A, we have the 1st and 2nd order Taylor expansions of intravoxel dephasing signal as follows

$$\begin{aligned} C[\mathbf{r},\mathrm{t}] \quad &\approx \frac{1}{|\Omega|}\sum_{\mathbf{r}'\in\Omega(\mathbf{r})}\left(1+i\gamma\cdot T_E\cdot b(\mathbf{r}',t)+\frac{(i\gamma\cdot T_E\cdot b(\mathbf{r}',t))^2}{2!}\right) \quad (2^{\text{nd}}\text{ Taylor expansion}) \\ &\approx \frac{1}{|\Omega|}\sum_{\mathbf{r}'\in\Omega(\mathbf{r})}(1+i\gamma\cdot T_E\cdot b(\mathbf{r}',t)) \qquad\qquad (1^{\text{st}}\text{ Taylor expansion}) \end{aligned} \tag{B2}$$

From (B2), we obtain the T2* magnitude signal at the 1st order approximation

$$\begin{aligned} A^{raw}[\mathbf{r},t] \quad &\approx \frac{1}{|\Omega|}\sum_{\mathbf{r}'\in\Omega(\mathbf{r})}\left(1+\frac{(\gamma\cdot b(\mathbf{r}',t)\cdot T_E)^2}{2}\right) \quad (1^{\text{st}}\text{ Taylor expansion}) \\ &= 1+\frac{(\gamma T_E)^2}{2|\Omega|}\sum_{\mathbf{r}'\in\Omega(\mathbf{r})}(b(\mathbf{r}',t))^2 \qquad (\text{quadratic nonlinearity}) \end{aligned} \tag{B3}$$

That is, in the least nonlinearity approximation at 1st order Taylor expansion, a T2* magnitude image exhibits a quadratic nonlinearity. Therefore, we conclude that the T2* magnitude signal is a nonlinear mapping of the fieldmap in all circumstances. In particular, the quadratic nonlinearity causes the magnitude non-negativity, which prevents a static/dynamic decomposition as illustrated by the inseparability of δb and b_0 in $(\delta b+b_0)^2 = (\delta b)^2+(b_0)^2+2\cdot\delta b\cdot b_0$. Furthermore, T2* magnitude imaging is irreversible (for $b(\mathbf{r})$ reconstruction) due to a nonlinear mapping like $|\pm 1| = 1$.

Meanwhile, the 1st and 2nd approximations of T2* phase signal (from (B2)) are given by

$$\begin{aligned} P[\mathbf{r},t] \quad &\approx \arctan\left(\frac{\gamma T_E b[\mathbf{r},t]}{1-(\gamma T_E)^2 b^2[\mathbf{r},t]/2}\right) \quad (2^{\text{nd}}-\text{order approx.}) \\ &\approx \gamma T_E b[\mathbf{r},t] \qquad\qquad (1^{st}-\text{order approx.}) \\ \text{with} \quad b[\mathbf{r}] &= \frac{1}{|\Omega|}\sum_{\mathbf{r}'\in\Omega(\mathbf{r})} b(\mathbf{r}') \quad (\text{intravoxel fieldmap average}) \\ b^2[\mathbf{r},t] &= \frac{1}{|\Omega|}\sum_{\mathbf{r}'\in\Omega(\mathbf{r})} b^2(\mathbf{r}',t) \end{aligned} \tag{B4}$$

which shows that T2* phase signal is nonlinearly related to the fieldmap in a general setting (at 2nd and higher expansions).

Supporting information

S1 Fig. T2* magnitude image slices in a snapshot volume at a time point t_1 (captured by a GRE-EPI sequence). The z number (in units of mm) is the slice distance from brain top.
(TIF)

S2 Fig. T2* phase image slices in a snapshot at a time point t_1 (captured by a GRE-EPI sequence).
(TIF)

S3 Fig. Brain full χ source slices in a reconstructed 3D $\chi[x,y,z,t_1]$ (a 3D χ reconstruction from Laplacian-unwrapped phase volume by CIMRI).
(TIF)

S4 Fig. Brain BOLD δχ source slices in a reconstructed 3D $\delta\chi[x,y,z,t_1]$ (a 3D δχ reconstruction from a 3D δP by CIMRI).
(TIF)

S5 Fig. Task-correlated 3D brain functional map from the EPI magnitude dataset. The 3D *tcorr fmap* was converted into z-scores.
(TIF)

S6 Fig. Task-correlated χ-depicted 3D brain functional map from a reconstructed 4D χ dataset (including brain background χ_0). The 3D *tcorr fmap* was converted into z-scores.
(TIF)

S7 Fig. Task-correlated δχ-depicted 3D brain functional map from a reconstructed 4D δχ dataset (excluding brain background χ_0). The 3D *tcorr fmap* was converted into z-scores.
(TIF)

S8 Fig. A χ-depicted brain cortex structure. Multiple axial slices from a reconstructed 3D χ volume (image enhanced).
(TIF)

S1 Data. S1Data.rar (compressed raw 7T magnitude, part 1 of 2 parts).
(RAR)

S2 Data. S2Data.rar (compressed raw 7T magnitude, part 2 of 2 parts).
(RAR)

S3 Data. S3Data.rar (compressed raw 7T phase, part 1 of 2 parts).
(RAR)

S4 Data. S4Data.rar (compressed raw 7T phase, part 2 of 2 parts).
(RAR)

S5 Data. S5Data.rar (compressed raw 3T magnitude, part 1 of 3 parts).
(RAR)

S6 Data. S6Data.rar (compressed raw 3T magnitude, part 2 of 3 parts).
(RAR)

S7 Data. S7Data.rar (compressed raw 3T magnitude, part 3 of 3 parts).
(RAR)

S8 Data. S8Data.rar (compressed raw 3T phase, part 1 of 3 parts).
(RAR)

S9 Data. S9Data.rar (compressed raw 3T phase, part 2 of 3 parts).
(RAR)

S10 Data. S10Data.rar (compressed raw 3T phase, part 3 of 3 parts).
(RAR)

Acknowledgments

The authors would like to acknowledge the funding support of NIHP20GM103472.

Author Contributions

Conceptualization: Zikuan Chen.

Data curation: Jennifer Robinson.

Formal analysis: Zikuan Chen, Vince Calhoun.

Funding acquisition: Vince Calhoun.

Investigation: Zikuan Chen, Vince Calhoun.

Methodology: Zikuan Chen.

Project administration: Vince Calhoun.

Resources: Vince Calhoun.

Software: Zikuan Chen.

Supervision: Vince Calhoun.

Validation: Zikuan Chen.

Visualization: Zikuan Chen.

Writing – original draft: Zikuan Chen.

Writing – review & editing: Zikuan Chen, Jennifer Robinson, Vince Calhoun.

References

1. Buxton RB (2010) Interpreting oxygenation-based neuroimaging signals: the importance and the challenge of understanding brain oxygen metabolism. Front Neuroenergetics 2: 8. https://doi.org/10.3389/fnene.2010.00008 PMID: 20616882
2. Buxton RB, Wong EC, Frank LR (1998) Dynamics of blood flow and oxygenation changes during brain activation: the balloon model. Magn Reson Med 39: 855–864. PMID: 9621908
3. Ogawa S, Menon RS, Tank DW, Kim SG, Merkle H, Ellermann JM, et al. (1993) Functional brain mapping by blood oxygenation level-dependent contrast magnetic resonance imaging. A comparison of signal characteristics with a biophysical model. Biophys J 64: 803–812. https://doi.org/10.1016/S0006-3495(93)81441-3 PMID: 8386018
4. Ogawa S, Tank DW, Menon R, Ellermann JM, Kim SG, Merkle H, et al. (1992) Intrinsic signal changes accompanying sensory stimulation: functional brain mapping with magnetic resonance imaging. Proc Natl Acad Sci U S A 89: 5951–5955. PMID: 1631079
5. Chen Z, Calhoun V (2013) Understanding the morphological mismatch between magnetic susceptibility source and T2* image. Magnetic Resonance Insights 6: 65–81. https://doi.org/10.4137/MRI.S11920 PMID: 25114545
6. Chavhan GB, Babyn PS, Thomas B, Shroff MM, Haacke EM (2009) Principles, techniques, and applications of T2*-based MR imaging and its special applications. Radiographics: a review publication of the Radiological Society of North America, Inc 29: 1433–1449.
7. Chen Z, Calhoun V (2015) Nonlinear magnitude and linear phase behaviors of T2* imaging: theoretical approximation and Monte Carlo simulation. Magn Reson Imaging 33: 390–400. https://doi.org/10.1016/j.mri.2015.01.016 PMID: 25623809
8. Chen Z, Calhoun V (2016) T2* phase imaging and processing for magnetic susceptibility mapping. Biomedical Physics and Engineering Express 2.
9. Haacke EM, Liu S, Buch S, Zheng W, Wu D, Ye Y (2015) Quantitative susceptibility mapping: current status and future directions. Magn Reson Imaging 33: 1–25. https://doi.org/10.1016/j.mri.2014.09.004 PMID: 25267705
10. Haacke EM, Ye Y (2012) The role of susceptibility weighted imaging in functional MRI. NeuroImage 62: 923–929. https://doi.org/10.1016/j.neuroimage.2012.01.020 PMID: 22245649
11. Boxerman JL, Bandettini PA, Kwong KK, Baker JR, Davis TL, Rosen BR, et al. (1995) The intravascular contribution to fMRI signal change: Monte Carlo modeling and diffusion-weighted studies in vivo. Magn Reson Med 34: 4–10. PMID: 7674897
12. Martindale J, Kennerley AJ, Johnston D, Zheng Y, Mayhew JE (2008) Theory and generalization of Monte Carlo models of the BOLD signal source. Magn Reson Med 59: 607–618. https://doi.org/10.1002/mrm.21512 PMID: 18224696

13. Pathak AP, Ward BD, Schmainda KM (2008) A novel technique for modeling susceptibility-based contrast mechanisms for arbitrary microvascular geometries: the finite perturber method. Neuroimage 40: 1130–1143. https://doi.org/10.1016/j.neuroimage.2008.01.022 PMID: 18308587
14. Chen Z, Calhoun V (2016) BOLD fMRI Simulation. In: Lipovic I, editor. Numerical Simulation. Croatia: InTech.
15. Chen Z, Calhoun V (2012) Volumetric BOLD fMRI simulation: from neurovascular coupling to multivoxel imaging. BMC Med Imaging 12: 8. https://doi.org/10.1186/1471-2342-12-8 PMID: 22524545
16. Chen Z, Calhoun V (2015) Intrinsic functional mapping in reconstructed 4D magnetic susceptibility data space J Neurosci Methods 241: 85–93. https://doi.org/10.1016/j.jneumeth.2014.12.014 PMID: 25546484
17. Chen Z, Calhoun VD (2011) Two pitfalls of BOLD fMRI magnitude-based neuroimage analysis: non-negativity and edge effect. Journal of Neurosci Methods 199: 363–369.
18. Chen Z, Liu J, Calhoun VD (2013) Susceptibility-based functional brain mapping by 3D deconvolution of an MR-phase activation map. Journal of Neurosci Methods 216: 33–42.
19. Sun H, Seres P, Wilman AH (2017) Structural and functional quantitative susceptibility mapping from standard fMRI studies. NMR Biomed 30.
20. Chen Z, Calhoun V (2012) Computed inverse resonance imaging for magnetic susceptibility map reconstruction. Journal of Computer Assisted Tomography 36: 265–274. https://doi.org/10.1097/RCT.0b013e3182455cab PMID: 22446372
21. Raichle ME (2010) Two views of brain function. Trends Cogn Sci 14: 180–190. https://doi.org/10.1016/j.tics.2010.01.008 PMID: 20206576
22. Gonzalez-Castillo J, Bandettini PA (2017) Task-based dynamic functional connectivity: Recent findings and open questions. Neuroimage.
23. Finn ES, Shen X, Scheinost D, Rosenberg MD, Huang J, Chun MM, et al. (2015) Functional connectome fingerprinting: identifying individuals using patterns of brain connectivity. Nat Neurosci 18: 1664–1671. https://doi.org/10.1038/nn.4135 PMID: 26457551
24. Vogt N (2015) fMRI goes individual. Nat Methods 12: 1112–1113.
25. Reitz JR, Milford FJ, Christy RW (1993) Foudations of electromagnetic theory. New York: Addison-Wisley.
26. Haacke EM, Brown R, Thompson M, Venkatesan R (1999) Magnetic resonance imaging physical principles and sequence design. New York: John Wiley & Sons, Inc.
27. Navarro MA, Estrada JC, Servin M, Quiroga JA, Vargas J (2012) Fast two-dimensional simultaneous phase unwrapping and low-pass filtering. Opt Express 20: 2556–2561. https://doi.org/10.1364/OE.20.002556 PMID: 22330493
28. Schofield MA, Zhu Y (2003) Fast phase unwrapping algorithm for interferometric applications. Opt Lett 28: 1194–1196. PMID: 12885018
29. Li W, Avram AV, Wu B, Xiao X, Liu C (2014) Integrated Laplacian-based phase unwrapping and background phase removal for quantitative susceptibility mapping. NMR Biomed 27: 219–227. https://doi.org/10.1002/nbm.3056 PMID: 24357120
30. Chen Z, Calhoun V (2014) 3D and 4D magnetic susceptibility tomography based on complex MR images. USA patent 8,886,283, B1.
31. Sepulveda NG, Thomas IM, Wikswo JP (1994) Magnetic Susceptibility Tomography for Three-dimensional Imaging of Diamagnetic and Paramagnetic Objects. IEEE Trans Magnetics 30: 5062–5069.
32. Tang J, Liu S, Neelavalli J, Cheng YC, Buch S, Haacke EM (2013) Improving susceptibility mapping using a threshold-based K-space/image domain iterative reconstruction approach. Magn Reson Med 69: 1396–1407. https://doi.org/10.1002/mrm.24384 PMID: 22736331
33. Wharton S, Schafer A, Bowtell R (2010) Susceptibility mapping in the human brain using threshold-based k-space division. Magn Reson Med 63: 1292–1304. https://doi.org/10.1002/mrm.22334 PMID: 20432300
34. Langkammer C, Bredies K, Poser BA, Barth M, Reishofer G, Fan AP, et al. (2015) Fast quantitative susceptibility mapping using 3D EPI and total generalized variation. Neuroimage 111: 622–630. https://doi.org/10.1016/j.neuroimage.2015.02.041 PMID: 25731991
35. Liu T, Liu J, de Rochefort L, Spincemaille P, Khalidov I, Ledoux JR, et al. (2011) Morphology enabled dipole inversion (MEDI) from a single-angle acquisition: comparison with COSMOS in human brain imaging. Magn Reson Med 66: 777–783. https://doi.org/10.1002/mrm.22816 PMID: 21465541
36. Liu T, Xu W, Spincemaille P, Avestimehr AS, Wang Y (2012) Accuracy of the morphology enabled dipole inversion (MEDI) algorithm for quantitative susceptibility mapping in MRI. IEEE Trans Med Imaging 31: 816–824. https://doi.org/10.1109/TMI.2011.2182523 PMID: 22231170

37. Li W, Wang N, Yu F, Han H, Cao W, Romero R, et al. (2015) A method for estimating and removing streaking artifacts in quantitative susceptibility mapping. Neuroimage 108: 111–122. https://doi.org/10.1016/j.neuroimage.2014.12.043 PMID: 25536496

38. Li W, Wu B, Liu C (2011) Quantitative susceptibility mapping of human brain reflects spatial variation in tissue composition. Neuroimage 55: 1645–1656. https://doi.org/10.1016/j.neuroimage.2010.11.088 PMID: 21224002

39. Chen Z, Calhoun V (2014) Reconstructing brain magnetic susceptibility distributions from T2* phase images by TV-reguarlized 2-subproblem split Bregman iterations. Reports in Medical Imaging 7: 41–53.

40. Cai J, Osher S, Shen Z (2009) Split Bregman Methods and Frame Based Image Restoration. Multiscale Model Simul 8: 337–369.

41. Magnotta VA, Friedman L, First B (2006) Measurement of Signal-to-Noise and Contrast-to-Noise in the fBIRN Multicenter Imaging Study. J Digit Imaging 19: 140–147. https://doi.org/10.1007/s10278-006-0264-x PMID: 16598643

42. Paul JS, Krishna Swamy Pillai U (2015) A higher dimensional homodyne filter for phase sensitive partial Fourier reconstruction of magnetic resonance imaging. Magn Reson Imaging 33: 1114–1125. https://doi.org/10.1016/j.mri.2015.06.005 PMID: 26117692

43. Balla DZ, Sanchez-Panchuelo RM, Wharton SJ, Hagberg GE, Scheffler K, Francis ST, et al. (2014) Functional quantitative susceptibility mapping (fQSM). Neuroimage 100: 112–124. https://doi.org/10.1016/j.neuroimage.2014.06.011 PMID: 24945672

44. Bianciardi M, van Gelderen P, Duyn JH (2014) Investigation of BOLD fMRI resonance frequency shifts and quantitative susceptibility changes at 7 T. Hum Brain Mapp 35: 2191–2205. https://doi.org/10.1002/hbm.22320 PMID: 23897623

45. Deistung A, Schweser F, Reichenbach JR (2016) Overview of quantitative susceptibility mapping. NMR Biomed.

46. Chen Z, Calhoun V (2016) Inverse MRI for tomographic magentic susceptibility reconstrucion. Computed Tomogaphy (www.smgebooks.com). Dover, DE: SM Group Open Access eBooks.